Janus organic semiconductor nanoparticles prepared by simple nanoprecipitation

A. Holmes, H. Laval, M. Schmutz, S. Blanc, Joachim Allouche, B. Watts, G. Wantz, N.P. Holmes, K. Hirakawa, Elise Deniau-Lejeune, et al.

Janus Organic Semiconductor Nanoparticles prepared by Simple Nanoprecipitation

Alexandre Holmes[1], Hugo Laval[2], Marc Schmutz[3], Sylvie Blanc[1], Joachim Allouche[1], Benjamin Watts[4], Guillaume Wantz[2], Natalie P. Holmes[5], Kazuhiko Hirakawa[6], Elise Deniau[1,7], Sylvain Chambon[6], Christine Lartigau-Dagron[1], Antoine Bousquet[1*]*

1: Universite de Pau et des Pays de l'Adour, E2S UPPA, CNRS, IPREM, Pau, France
2: University of Bordeaux, IMS, CNRS, UMR 5218, Bordeaux INP, ENSCBP, F-33405 Talence, France
3: Université de Strasbourg, CNRS, Institut Charles Sadron-UPR22, rue du Loess Strasbourg
4: Paul Scherrer Institute, 5232 Villigen-PSI, Switzerland
5: Australian Centre for Microscopy and Microanalysis, The University of Sydney, Madsen Building F09, NSW 2006, Australia
6: LIMMS/CNRS-IIS (IRL2820), Institute of Industrial Science, The University of Tokyo, 4-6-1 Komaba, Meguro-ku, Tokyo, 153-8505, Japan
7: Institut des Molécules et Matériaux du Mans, UMR CNRS 6283, Le Mans Université, 72085 Le Mans Cedex 9, France.

*Corresponding authors: christine.lartigau-dagron@univ-pau.fr , antoine.bousquet@univ-pau.fr;

KEYWORDS: π-conjugated materials, Janus nanoparticles, Photocatalysis, Photovoltaics

ABSTRACT: Nanoparticles of donor-acceptor organic semiconductors are produced by a one-step nanoprecipitation with a Janus morphology. Electron donor P3HT was blended with electron acceptor $PC_{61}BM$ in THF and then precipitated in water, firstly with surfactant, and secondly without surfactant. Cryo-TEM reveals an internal Janus structure at high magnification, for nanoparticles which have, in the past, been reported to have a molecularly intermixed morphology. Synchrotron-based scanning transmission X-ray microscopy (STXM) confirmed the segregation of the organic semiconductors and photoluminescence experiments showed an efficient electron transfer from P3HT to $PC_{61}BM$. Organic field effect transistors (OFETs) were fabricated with these Janus nanoparticles and showed that the positive charges can be efficiently transported through thin films. This behaviour proves that the nanoparticles

possess an electron-accepting face (the $PC_{61}BM$ face) able to transport electrons and a hole-accepting face (the P3HT face) for the conduction of holes. Finally, the deposition of silver *via* the photoreduction of a silver salt ($AgNO_{3(aq)}$) was demonstrated, as a proof of concept. These experiments show the potential of the Janus nanoparticles for photovoltaics but also photocatalytic reactions in which reduction and oxidation reactions can occur at opposite sides of the nanoreactor (the individual Janus nanoparticles).

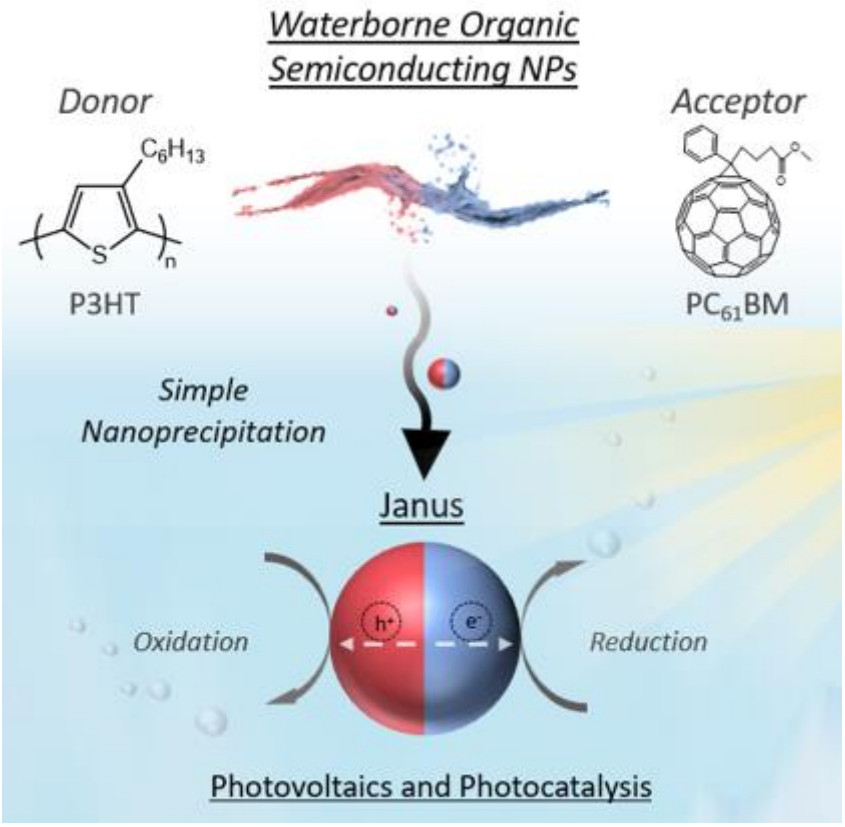

1. Introduction

The sun's photons provide the largest source of energy on earth and its exploitation will contribute to solve the world energy crisis without being detrimental for the environment. Indeed, photovoltaics (PV) technology allows the transformation of photons into electricity.[1,2] Additionally, hydrogen (H_2) production *via* photocatalytic water splitting has emerged as an attractive solution to store solar energy in a dispensable fuel that does not generate carbon dioxide (CO_2), neither at the fabrication nor consumption stages.[3] Further, artificial photosynthesis is being developed to use sunlight to provide electrons for the reduction of CO_2 in order to produce other solar fuels like ethanol.[4,5] The development of organic semiconductor nanoparticles has received significant consideration in the past three decades for these applications.[6–8] Organic semiconductors, either polymers (mostly electron donor) or small molecules (fullerene derivatives or non-fullerene acceptors), can be dispersed in water to provide human and environmentally-friendly fabrication processes for organic photovoltaic (OPV) devices as an alternative to classical options which are typically using toxic organic solvent, such as chloroform and dichlorobenzene.[9] Concerning solar fuels production, Pinaud *et al.* applied life cycle analysis to the production of H_2, demonstrating that a colloidal system, in which the photocatalysts are in the form of nanoparticles (NPs) dispersed in water, would be the cheapest technology compared to planar photoelectrodes.[10]

Self-assembly is a straightforward methodology to obtain organic nanoparticles dispersed in water. The driving force for the self-assembly is a decrease of surface energy, resulting in the segregation of all components towards an overall thermodynamic equilibrium. As a consequence, the morphology of a multicomponent nanoparticle evolves during segregation. Moreover, it has been thoroughly documented that the donor/acceptor morphology is a critical parameter in the OPV field.[11–13] Nanoscale domain size that closely matches exciton diffusion

length (approximately 10-20 nm) and conduction pathways for charges are both required to maximize performances.

A core-shell morphology is classically reported when miniemulsion is used for the nanoparticle preparation.[6,9] Donor and acceptor materials segregate in the miniemulsion hydrophobic droplets to minimize interface energy with water (or surfactant/water), while the organic solvent is slowly evaporating. Since the evaporation time is long, one of the components segregates to the core of the particles, while the other component forms the shell. Several organic semiconductor nanoparticle dispersions have been reported in the literature with a core-shell morphology such as TQ1:$PC_{71}BM$,[14] P3HT:$PC_{61}BM$,[15] P3HT:N2200 and TQ1:N2200.[16] However, several studies reported device performance limitations due to this morphology, either for PV or H_2 production, because after exciton dissociation, electrons or holes can be trapped in the core, without having the possibility to respectively reach the electrodes or the aqueous medium.[7,17,18]

Molecularly intermixed morphology is the second type of reported internal structure for organic semiconductor nanoparticles, which is mostly obtained *via* the nanoprecipitation methodology.[9] During the nanoparticle formation, the rapid diffusion of the organic solvent (water/alcohol miscible) into the non-solvent leaves such little time for the donor and acceptor material to segregate, that a molecularly intermixed structure is obtained. This morphology was reported by different groups for P3HT:$PC_{61}BM$ (in ethanol),[19] P3HT:ICBA (in alcohols),[20] and PCDTBT:$PC_{71}BM$ (in water).[21] The enhanced PV performances compared to the core-shell dispersion were attributed to better electron extraction. Kosco *et al.* recently showed that this intermixed morphology was also superior for hydrogen solar fuel production, improving the H_2 evolution rate from 3,000 μmol $h^{-1}g^{-1}$ to 28,000 μmol $h^{-1}g^{-1}$, compared to the core-shell morphology.[7]

In this report, we demonstrate the one-step formation of Janus nanoparticles, the simplest multifaced nanoparticle named after the two-faced Roman god, Janus, made of semiconducting organic materials *via* nanoprecipitation. Clear segregation between poly(3-hexylthiophene (P3HT) and [6,6]-phenyl-C_{61}-butyric acid methyl ester ($PC_{61}BM$) has been observed by cryogenic transmission electron microscopy (cryo-TEM) and synchrotron-based scanning transmission X-ray microscopy (STXM). Photoluminescence spectroscopy showed that the emission from the donor material is efficiently quenched. Organic field effect transistors (OFET) were prepared with Janus P3HT:$PC_{61}BM$ NP to demonstrate that the charges produced are efficiently transported to the electrodes. Finally, the deposition of silver *via* the photoreduction of a silver salt ($AgNO_{3(aq)}$) was demonstrated. These results open the way to direct application in PV and in photocatalysis for the production of solar fuels.

2. Material and Methods

2.1. Nanoparticles synthesis

Commercial P3HT (50K Solaris) and $PC_{61}BM$ (Sigma) are first solubilized in tetrahydrofuran (THF) at 65°C for at least 2 hours. The aqueous phase is prepared by adding (if required) SDS or Pluronic F127 in MilliQ Water, and stirred few minutes. In a round bottom flask of 25 mL, 16 mL of the aqueous solution are injected (filtered on a cellulose filter of 0.45 µm in order to avoid any dust). Right before the addition of the organic solution, the aqueous medium is stirred at 650RPM, for at least 30 seconds, to ensure that the vortex is stable. Then, the organic solution (maintained at 65°C) is introduced quickly in the aqueous medium, under stirring, leading to the instantaneous formation of a red/purple dispersion. In order to eliminate THF, the stirring rate is reduced to 300 RPM, the dispersion is heated up to 70°C with a nitrogen airflow, for at least 1 hour (depending on the volume of organic solvent).

Dispersions stabilized with surfactant can be concentrated through centrifugal dialysis. AmiconR ultra-15 Centrifugal Filter Devices (cutoff 100Kg.mol-1) are used. A volume up to 12 mL of the dispersion is added in the centrifugation tube, and then centrifugation using a Beckman Coulter Avanti J-30I centrifuge, at 6400 RPM (5,000 G) for 12 minutes in order to reduce the volume up to 200 µL. For dispersions using Pluronic F127, the dispersion is first cooled down to 0°C, and the centrifugation step is performed at 2°C, in order to efficiently remove the surfactant excess. This step was repeated for at least 3 times, with the addition of MilliQ water between washing steps.

2.2. Photodeposition

P3HT:$PC_{61}BM$ NPs (0.3 mg), stabilised by F127 (excess removed by centrifugal dialysis), $AgNO_3$ (1 mg) and methanol (100 µL) were mixed in a 5.2 mL aqueous solution. The medium was then irradiated with a THORLABS M450LP1 lamp at 450 nm for 4 hours. Dialysis in extra pure water was performed in order to remove the excess of $AgNO_3$ and methanol.

2.3. Characterization

Dynamic light scattering (DLS). The hydrodynamic diameters Dh and polydispersity (PDI) of particle dispersions were measured by DLS on a Nano-ZS zetasizer (Model ZEN3600 Malvern Instruments) operating at an angle of 173°. Nano-ZS is equipped with a He-Ne 4.0 mW power laser operating at a wavelength of 633 nm. The particles were dispersed in deionized water at a concentration of 0.05 $g.L^{-1}$. The data were calculated using the cumulant analysis.

Cryogenic transmission electron microscopy (Cryo-TEM). A drop of 5 µL of the solutions was applied to a copper grid covered with a carbon film made hydrophilic using an ELMO glow

discharge device (Cordouan Technologies, France). The grid was placed in a home-made vitrification apparatus at 22°C and 80% relative humidity before plunging into liquid ethane maintained at -190°C by liquid nitrogen. The grid was mounted on a cryo holder (Gatan 626, USA) and observed in a Tecnai G2 microscope (FEI, The Netherlands) at 200 kV. Images were acquired using an Eagle slow scan CCD camera (FEI).

Near Edge X-ray Absorption Fine Structure (NEXAFS) measurements of P3HT and $PC_{61}BM$ were performed on the PolLux beamline (X07DA) at the Swiss Light Source (SLS) synchrotron. Pristine films of P3HT and PC61BM were prepared by spin coating chloroform and chlorobenzene solutions, respectively, of each semiconductor material onto PEDOT:PSS coated glass substrates. 2 x 2 mm^2 sections were scored on the films using a scalpel, followed by floating off the film sections onto a D.I. water surface, which was made possible by dissolving the PEDOT:PSS sacrificial layer under the semiconductor material films. 2 x 2 mm^2 film sections were subsequently collected onto 300 mesh Cu grids (20 mm bar, 63 mm hole, 3 mm diameter, purchased from ProSciTech Pty Ltd) for NEXAFS measurements. The energy of the X-ray beam was varied between 278 and 390 eV, spanning the C K-edge region. Second- and third-order light was removed by an order sorting aperture and higher order suppressor. Orthogonal energies were determined from NEXAFS spectra of pristine films of P3HT and $PC_{61}BM$.

X-ray spectromicroscopy (STXM) measurements were performed on the PolLux beamline (X07DA) at the SLS synchrotron. Samples were prepared for STXM measurements by spin coating 2.5 μL of nanoparticle dispersions onto low stress silicon nitride (Si_3N_4) membrane windows (window dimensions 1 x 1 mm^2, window thickness 30 nm, silicon frame dimensions 5 x 5 mm^2, purchased from Silson, UK) at 3000 rpm, 1 min, low acceleration. Samples were air dried at room temperature. The samples on Si_3N_4 windows were loaded in the STXM sample chamber and rastered with respect to the X-ray beam. The transmitted X-ray beam is detected

by a scintillator and a photomultiplier tube. The STXM Fresnel zone plate (Ni) had an outer most zone width of 25 nm, setting the spatial resolution limit of the measurement. Singular value decomposition (SVD) was used to fit a sum of the pristine material NEXAFS spectra to the measured blend spectrum of the nanoparticles, at each pixel, in the STXM images. Prior to SVD fitting, the pristine material NEXAFS spectra were normalized to film thickness. The method of reference-spectrum normalization constitutes dividing the real spectrum by a theoretical spectrum calculated based on the material's chemical formula using henke.lbl.gov/optical_constants/filter.html. The aXis2000 package was used to perform image analysis of STXM maps.

Correlative TEM enabled position-matched STXM-TEM images to be generated. Following STXM mapping at the Swiss Light Source, the Si_3N_4 substrates with deposited nanoparticles were transported back to the University of Newcastle (Australia) for TEM measurements on a JEOL 1200 EXII at an accelerating voltage of 80 kV.

UV–visible absorption spectra of P3HT:$PC_{61}BM$ nanoparticles were recorded on a Shimadzu UV-2450PC spectrophotometer. Emission Spectroscopy (Photoluminescence): The corrected steady-state luminescence spectra were measured between 520 and 800 nm at 2 nm resolution using a photon counting Edinburgh FLS920 fluorescence spectrometer equipped with a Xenon lamp. The concentrations of all compounds in MilliQ Water were adjusted to give an absorbance around 0.1 at the excitation wavelength (510 nm) in a 1 cm fluorescence quartz optical cell (Hellma).

OFET devices were fabricated base on a bottom-gate top-contact structure. N-doped Si wafers with 230 nm-thick thermally grown SiO_2 were purchased from Fraunhofer IPMS. Substrates were cleaned by sequential ultrasonic treatments of 10 minutes at 50°C: acetone, ethanol and isopropanol. No passivation layers were used. Prior to deposition of the active layer, substrates were treated by UV-ozone for 15 minutes. The active layers were obtained by spin coating with

a rotation speed of 1300 RPM, in order to have a homogeneous film formation. After deposition of the P3HT:$PC_{61}BM$ thin film, thermal evaporation of gold electrode was performed through a shadow mask to define the source and drain electrodes using ULVAC thermal evaporator. Four kind of channel length (L) were defined: 50, 75, 100 and 125 µm for 1.5 mm channel width (W). OFET devices were connected from the back side to a copper plate using silver paste.

Auger electron spectroscopy (AES) were carried out with a JEOL JAMP 9500F Auger spectrometer nanoprobe (JEOL Ltd, Tokyo, Japan) equipped with a Schottky field emission gun working under UHV conditions (pressure < 2 .107 Pa). The AES spectra were recorded at a kinetic energy window from 0 to 800 eV by focusing the electron beam (size ≈ 10 nm, 20 keV, 5 nA) on target nanoparticles. The operating mode was a constant retarding ratio (CRR) mode for which the energy resolution (dE) linearly increases with the measured electron energy (E).

3. Result and Discussion

3.1. Nanoparticles synthesis

The nanoprecipitation technique relies on the miscibility of the organic solvent, in which the organic semiconductors are solubilized, and the aqueous phase acting as the anti-solvent, which can contain a surfactant. Upon addition of the solvent into the anti-solvent, a solvent displacement step occurs as the two are completely miscible, leading to the rapid precipitation of the hydrophobic materials into nanoparticles. This process is decomposed into three steps: nucleation, growth by accumulation and growth by coagulation.[22] An efficient stirring is therefore required in order to have homogeneous nucleation and growth steps in the entire volume, leading to small, monodisperse and stable nanoparticles.[21] As a starting point of this

study, a dispersion of P3HT:$PC_{61}BM$ (1:1, mass equivalent) was prepared from a THF solution at 2 $mg.mL^{-1}$ and a solvent/anti-solvent (THF/water) volume ratio of 1/8 (Entry 1, **Erreur ! Source du renvoi introuvable.**). The nanoprecipitation produced a colloidal dispersion with a mean particle hydrodynamic diameter, measured by DLS, of 100 nm. The dispersion was concentrated by centrifugal dialysis and the maximum solids content reached without irreversible aggregation was 1 $mg.mL^{-1}$. This low solids content will ultimately limit the use of this type of dispersion for solar cell fabrication where at least 20 $mg.mL^{-1}$ solution concentrations are usually required.

Table 1. P3HT:$PC_{61}BM$ nanoparticle dispersion characteristics.

Entry	Volume ratio	[P3HT:$PC_{61}BM$] ($mg.mL^{-1}$)	Surfactant	[Surfactant] ($mg.mL^{-1}$)	[NPs][a] ($mg.mL^{-1}$)	D_h[b] (nm)	PDI[b]
1	1/8	2.0	None	-	1.00	100	0.10
2	1/4	2.0	SDS	3.0	> 10	81	0.12
3		1.0	F127	3.0	> 10	68	0.18
4		2.0			> 10	79	0.14
5		5.0		0.5	> 10	131	0.08

[a] Final dispersion concentration used for cryo-TEM experiments;
[b] *Z*-average hydrodynamic diameter and particle polydispersity obtained by DLS using cumulant analysis.

With the objective of increasing the solids content of the dispersion, sodium dodecyl sulphate (SDS) or Pluronic F127 surfactants were added to the formulation, in the anti-solvent (water). Starting with the same photoactive materials concentration of 2 $mg.mL^{-1}$, and with a surfactant concentration of 3 $mg.mL^{-1}$, the mean particle diameter decreased to 80 nm (Entry 2 and 4, Table 1 for SDS and F127, respectively). The dispersion was then concentrated by the same centrifugation/filtration cycles and this time the solids content could be increased to over 10 $mg.mL^{-1}$ without aggregation, due to the addition of surfactants (note that the concentration can be increased up to 60 $mg.mL^{-1}$ without aggregation, but a concentration of 10 $mg.mL^{-1}$ was more suited for cryo-TEM experiments, see Supplementary Information for the procedure). This latter centrifugation/filtration step was also used to eliminate the excess of free surfactants

from the dispersion (see Supplementary Information) in order to decrease their possible negative impact on the PV device performance (insulating behaviour, charge traps, recombination centres, etc.).[23]

3.2. Nanoparticles morphology

The morphology of the nanoparticles was assessed by cryo-TEM in order to observe the structure in their native water-dispersed state. Due to its higher electron density (1.5 $g.cm^{-3}$), $PC_{61}BM$ appears darker than P3HT (1.1 $g.cm^{-3}$)[24] in micrographs reported in Figure 1 (arrows). For the three formulations defined above, *i.e.* without surfactant, or using SDS or F127 (Figure 1a-c), a Janus morphology was observed with P3HT and $PC_{61}BM$ clearly phase segregated from one another. A fine observation of the nanoparticles brings more information. First of all, the Janus domains are not completely pure and small dots of less than 10 nm are visible, meaning that nanodomains of $PC_{61}BM$ exist in the P3HT face and P3HT nanodomains exist in the $PC_{61}BM$ face (see additional cryo-TEM micrographs in Supplementary Information). Secondly, even though the mass ratio between P3HT and $PC_{61}BM$ is 1:1 and the volume ratio 1.36:1 (see calculation in Supplementary Information), the volume attributed to the P3HT bright areas appears much larger than the $PC_{61}BM$ dark areas.[24] Finally, the crystallinity of P3HT domains can be observed in the bright face of the Janus nanoparticles for each sample (Supplementary Information Figure SI-8), with striped areas characteristic of lamellar stacking of regioregular P3HT polymer chains.[25]

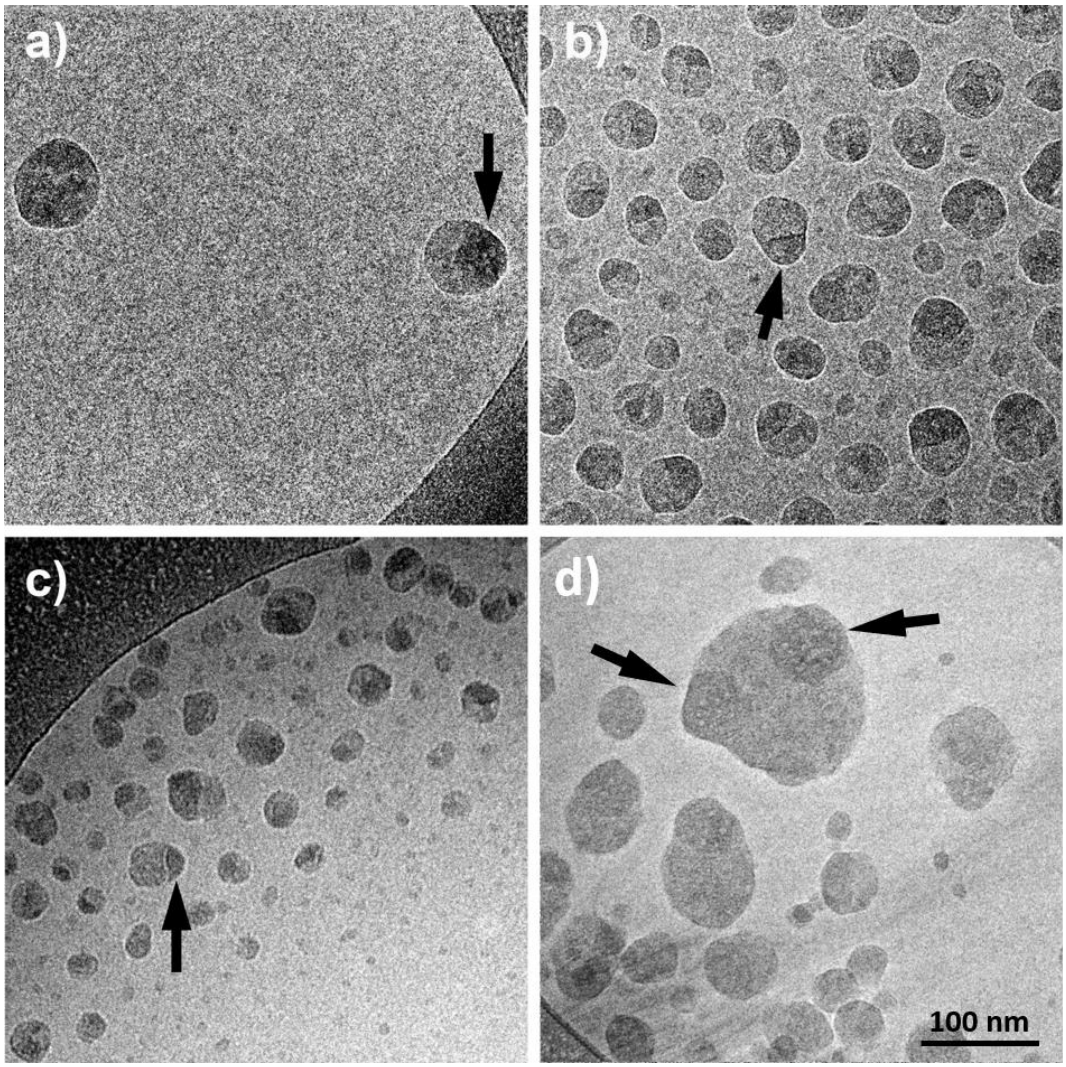

Figure 1. Cryo-TEM images of the nanoparticles a), b), c) and d) have been prepared from conditions listed in Table 1, Entry 1, 2, 4 and 5 respectively. The arrows point towards the $PC_{61}BM$ rich areas.

The formation of Janus-like nanoparticles *via* nanoprecipitation has already been reported in the literature for dispersions prepared from blends of two non-conjugated homopolymers such as PS/PI, PS/PB, PB/PLA.[26–28] In each case, the two polymers self-organized into hemispherical domains in order to minimize the system (polymer−polymer−liquid) interfacial energy. The Janus morphology emerged because the two polymers had similar interfacial energies with the liquid phase and a low interfacial energy between themselves. Modelling

studies confirmed that the formation of such nanoparticle morphology is intimately related to the interaction parameters between component A, component B and the liquid but also to the extremely quick formation of nanoparticles during the nucleation stage of the nanoprecipitation mechanism.[29] As soon as the organic phase diffuses through water, the active materials start to reach a supersaturated state, leading to the nucleation of active material all over the medium, as schematized in **Erreur ! Source du renvoi introuvable.**a.[22,30–32]

Concerning the particles prepared without surfactant, the liquid phase is composed, at the nucleation stage, of a THF/water mixture (1/8 v, Table 1, Entry 1) with a surface tension already reported as γ_{Liq} = 44.2 mN.m^{-1}.[33] The contact angles between films of P3HT or $PC_{61}BM$ and a drop of THF/water mixture were measured and the solid/liquid surface tensions, $\gamma_{PCBM/Liq}$ and $\gamma_{P3HT/Liq}$, were calculated (see Supplementary Information). These analyses show that $PC_{61}BM$ and P3HT have a similar solid/liquid surface tension, $\gamma_{PCBM/Liq}$ = 15.2 mN.m^{-1} and $\gamma_{P3HT/Liq}$ = 22.0 mN.m^{-1}, indicating that the nucleation is expected to occur simultaneously.[28] The inner morphology of the nuclei has been modelled to be dependent on the ratio between $\gamma_{PCBM/Liq}/\gamma_{P3HT/PCBM}$ and $\gamma_{P3HT/Liq}/\gamma_{P3HT/PCBM}$.[29] From the dispersive and polar component of the surface tension of the materials, the interfacial tension between P3HT and $PC_{61}BM$, $\gamma_{P3HT/PCBM}$, was calculated to be 13.6 mN.m^{-1} (see Supplementary Information) leading to a $\gamma_{PCBM/Liq}/\gamma_{P3HT/PCBM}$ of 1.12 and $\gamma_{P3HT/Liq}/\gamma_{P3HT/PCBM}$ of 1.62. Since the difference between these two last values is rather small, the predicted morphology is Janus with a larger surface domain of P3HT.[29] The $\gamma_{PCBM/Liq}/\gamma_{P3HT/PCBM}$ and $\gamma_{P3HT/Liq}/\gamma_{P3HT/PCBM}$ were also calculated for the other aqueous phases used in this study (SDS, F127 solutions). The difference between both values ($\gamma_{PCBM/Liq}/\gamma_{P3HT/PCBM}$ and $\gamma_{P3HT/Liq}/\gamma_{P3HT/PCBM}$) is small for all the tested conditions (Table S5 in Supplementary Information) and should also give rise to a Janus morphology in accordance with the model and cryo-TEM results.

Once the concentration of active materials in the mixed organic phase decreases below the supersaturation state, a step of nuclei growth occurs, by accumulation of the solubilized active materials (Figure 2a). Due to the incompatibility between the active materials, P3HT is more likely to accumulate preferentially on a P3HT-rich "face" of the nuclei, and $PC_{61}BM$ on a $PC_{61}BM$-rich face. Both steps of nucleation and growth occur extremely quickly. This was experimentally observed, with dynamic light scattering (DLS) analysis performed immediately after the addition of THF in water at t0 + 1 min., and after THF evaporation at t0 + 120 min. (see Supplementary Information Figure SI-11) showing the same particles size.

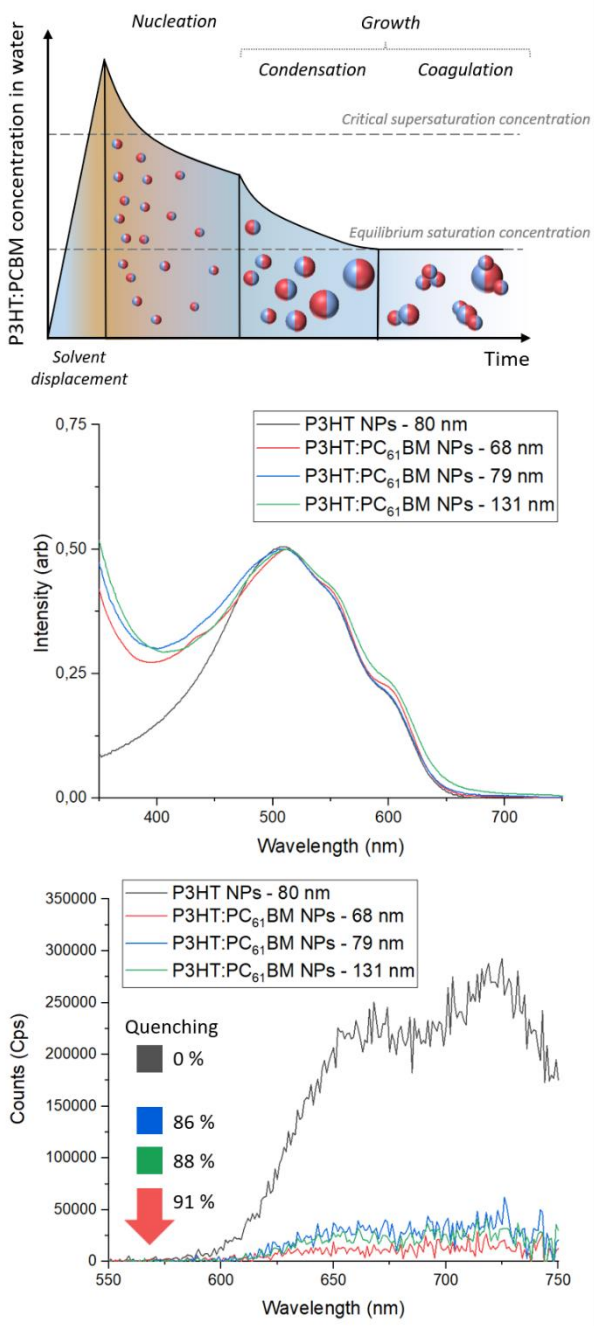

Figure 2. a) Scheme of the nanoparticle formation mechanism during nanoprecipitation, decomposed into three steps: nucleation, growth by condensation and growth by coagulation. Adapted with Janus nanoparticle from Martinez Rivas *et al.*[22] b) UV-visible spectra of P3HT and P3HT:PC_{61}BM NPs for different nanoparticle size. c) Evolution of the photoluminescence quenching of P3HT (excitation at 510 nm) for different nanoparticle sizes, all stabilized with F127

(Entry 3, 4, 5, Table 1). The quenching percentage was calculated from the count ratio between the P3HT reference and corresponding P3HT:$PC_{61}BM$ nanoparticles, between 630 and 750 nm.

The TEM image in Figure 1d represents the formulation of Table 1 Entry 5 in which the initial active materials concentration [P3HT:$PC_{61}BM$] was increased to 5 $mg.mL^{-1}$ and the surfactant concentration [F127] was decreased to 0.5 $mg.mL^{-1}$ in an attempt to produce larger nanoparticles. The mean hydrodynamic diameter of the spheres increased up to 131 nm (measured by DLS) and the TEM images showed the blend of small Janus nanoparticles with larger multifaced nanoparticles composed of one large P3HT domain and several $PC_{61}BM$ darker domains. We attributed this blend of morphologies to the coagulation of small Janus nanoparticles (Figure 2a) to give birth to large aggregates, this being induced by the increase of the active material/surfactant ratio. We believe that this step of growth by coagulation does not occur if collisions between Janus nanoparticles are impeded by the presence of a surfactant in sufficient concentration (Entry 2, 3, 4, Table 1) or if the solids content is low (Entry 1, Table 1). The nanoparticle size did not have a strong influence over the final material absorption, according to the UV-visible spectrum (Figure 2b). Only a slight increase of the shoulder at 600 nm can be observed for large nanoparticles, probably due to an increase of π-π stacking.

STXM measurements were performed at the PolLux beamline of the Swiss Light Source synchrotron (measurements details provided in the Supplementary Information)[34] to determine the morphology of the P3HT:$PC_{61}BM$ nanoparticles. STXM composition maps of P3HT:$PC_{61}BM$ (1:1) nanoparticles produced with and without surfactant (Entry 5 and 1 in Table 1) are presented in Figure 3. Although the observation was difficult due to the small nanoparticle size, no core@shell morphology was observed in the two sample types, consistent with the previous results reported for nanoparticles prepared via nanoprecipitation. Rather, several high contrast striped regions can be observed, indicative of alternating P3HT-rich and

$PC_{61}BM$-rich domains of Janus nanoparticles (framed in Figure 3), or agglomerations thereof. The presence of Pluronic F127 does not influence the nanoparticle morphology (additional maps depicting the nanoparticle morphology are provided in Supplementary Information in a 2-color map mode, Figure SI-9).

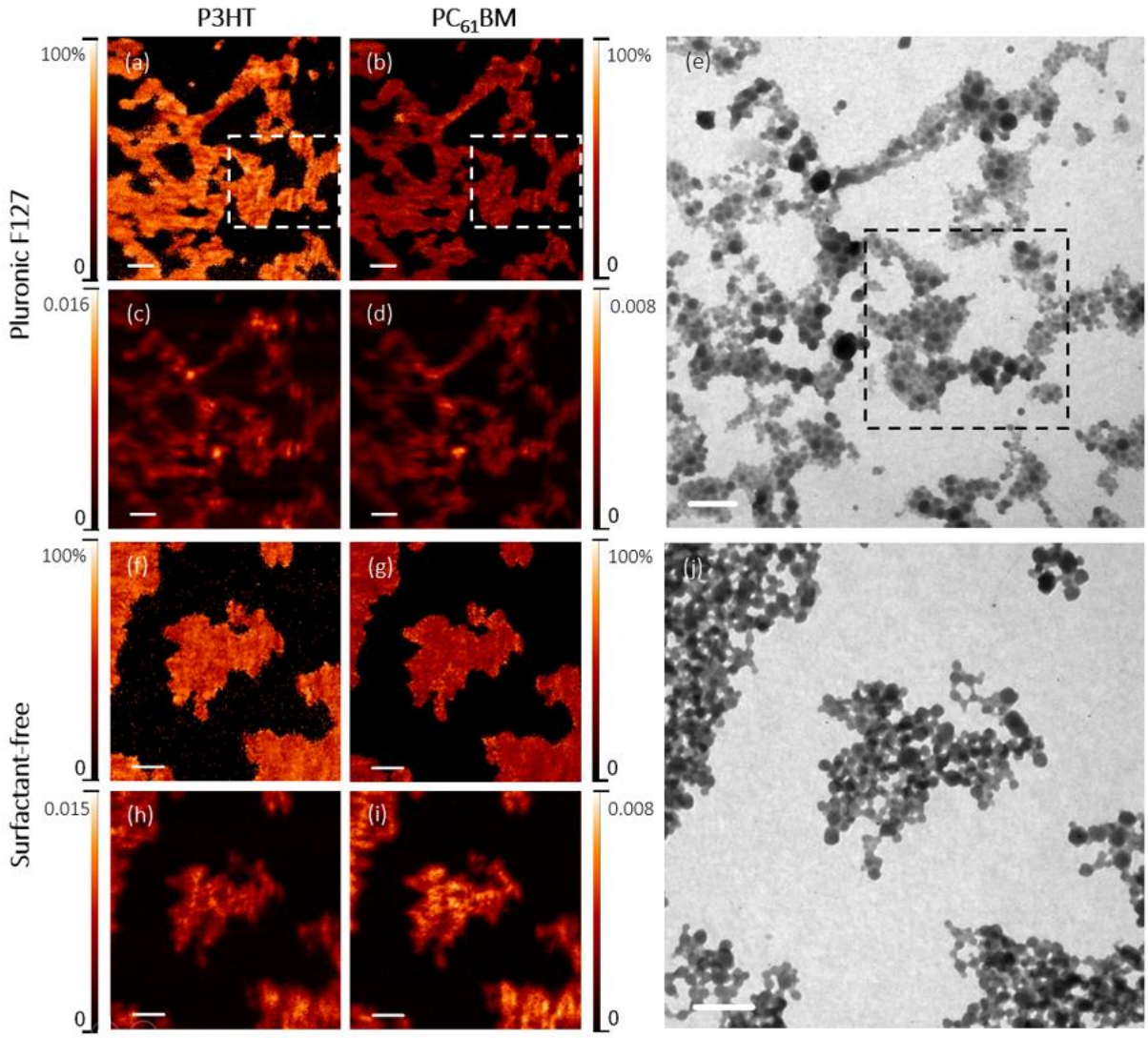

Figure 3. STXM fractional composition maps showing the concentration of P3HT (a) and $PC_{61}BM$ (b) with corresponding STXM mass plots (c and d) and correlative TEM (e) for 1:1 P3HT:$PC_{61}BM$ nanoparticles stabilized with Pluronic F127. STXM fractional composition maps showing the concentration of (f) P3HT and (g) $PC_{61}BM$ with corresponding STXM mass plots (h and i) and correlative TEM (j) for 1:1 P3HT:$PC_{61}BM$ surfactant-free nanoparticles. All scale bars are 500 nm. In STXM maps a-d and f-i, the colour contrast is scaled such that light colours correspond to

higher component concentrations. For the STXM mass plots (c, d, h, i) the colour scale bars indicate concentration of component in mg.cm^{-2}.

3.3. Optoelectronic properties

In order to investigate the exciton dissociation efficiency, the Janus nanoparticles were characterized by photoluminescence and compared with pristine P3HT nanoparticles (Figure 2c and further spectra in Supplementary Information). All P3HT:$PC_{61}BM$ nanoparticles showed a strong decrease in the P3HT emission (excitation wavelength at 510 nm) of at least 86% due to ultrafast electron transfer from P3HT to $PC_{61}BM$. The smallest nanoparticles (68 nm) quenched slightly more efficiently (94%) than the largest ones (86 and 89%), which is consistent with the existence of smaller material domains. When the particle diameter increases from 79 to 131 nm, the quenching is in the same range (86 and 89%). This is suggesting that the material domains size remains similar, which is explained by the formation mechanism *via* coagulation, detailed above and in Figure 2a, concerning the largest particles (131 nm). This important quenching behaviour indicates a high exciton dissociation rate within these particles. This opens the way for the use of these dispersions in solar technologies, where donor-acceptor interfaces for exciton dissociation are needed.

As mentioned in the introduction, other research teams have reported an intermixed morphology for nanoparticles made *via* nanoprecipitation rather than the Janus morphology reported here.[19–21,35] This difference can come from several factors. First of all, it is possible that these previous works actually produced Janus particles, but that the microscopic characterisation by microscopy was not performed with a sufficient spatial resolution to distinguish Janus from the intermixed morphology, or the two materials didn't show enough contrast (in TEM, SEM or AFM). Photoluminescence was also used to prove quenching. However, PL is not a suitable technique to discriminate between intermixed or Janus

morphology (at least when the size of the nanoparticles is below 100 nm). Secondly, previous works of nanoprecipitation did not use surfactant and hence aggregation by coagulation could have induced the creation of larger multidomain nanoparticles such as those shown in Figure 1d) and therefore obscured the small-scale morphology, especially when characterising large nanoparticles. Finally, some groups used ethanol rather than water as the anti-solvent so the $\gamma_{solid/liquid}$ values differ from those in the present study and may have produced a different morphology.

In order to probe the charge transport in these Janus NPs, organic field effect transistors have been prepared with P3HT:PC_{61}BM NPs (F127, Table 1, entry 3) and following a bottom-gate top-contact architecture on Si/SiO_2 wafers (n-doped Si/ SiO_2/P3HT:PC_{61}BM/Au). A reference P3HT:PC_{61}BM device was casted from chlorobenzene. Both layers, deposited from NP or from organic solvent, were then annealed at 120°C for 10 minutes in glovebox. Details of transistors preparations and characterisation are given in SI.

Hole mobilities (μ_{h+}) were extracted from the transfer characteristic ($I_{DS}=f(V_{GS})$) in the saturation regime[36] (Figure SI-14) for P3HT:PC_{61}BM thin films casted from organic solvent as well as for P3HT:PC_{61}BM NP assemblies. The devices show a hole mobility about 4.9 10^{-5} $cm^2.V^{-1}.s^{-1}$, against 3.2 10^{-5} $cm^2.V^{-1}.s^{-1}$ for the reference samples casted from chlorobenzene and aqueous dispersions respectively. Therefore, the hole transport trough P3HT:PC_{61}BM NP assemblies appears to be as efficient as in P3HT:PC_{61}BM thin film casted from organic solvent. However, the hole mobility in P3HT:PC_{61}BM NP is one order of magnitude lower than the value obtained with only P3HT NP assemblies, casted from aqueous dispersions (μ_{h+} = 1.2 10^{-4} $cm^2.V^{-1}.s^{-1}$) see Figure SI-13). Such difference indicates that the presence of $PCB_{61}M$ hinders the conduction pathways of between P3HT domains, resulting in a lower hole mobility. More investigation must be performed to understand the impact of the size and thermal treatment of

these P3HT:$PC_{61}BM$ Janus NPs on the charge transport since high and equilibrated mobilities are some of the conditions to achieve high performances organic photovoltaic devices.[37,38]

Finally, the potential for photocatalysis of these Janus nanoparticles was revealed *via* the successful elaboration of hybrid nanoparticles by photodeposition. For this purpose, the P3HT/$PC_{61}BM$ dispersions stabilized by F127 were irradiated at λ = 450 nm in the presence of $AgNO_{3(aq)}$ and a sacrificial electron donor, methanol. The objective was to reduce Ag^+ with the photogenerated electrons coming from the Janus nanoparticles. Indeed, the laser irradiation (450 nm) absorbed by P3HT promotes the exciton dissociation (already proved by photoluminescence) and should produce electrons that are sufficiently reducing to transform Ag^+ into silver metal. As a consequence, silver metallic aggregates should deposit at the surface of the organic nanoparticles, as schematically represented on Figure 4a.

The presence of silver was first suggested by DLS, with an increase in the nanoparticle diameter, from 85 to 157 nm, after laser irradiation but also by an increase in the UV-Vis absorbance around 450 nm, classically attributed in literature to Ag nanoparticles (see Supporting Information Figure SI-15).[39] For further evidence, nanoparticles were imaged via Cryo-TEM, and Figure 4b displays dark features corresponding to silver metal deposited on organic semiconductor nanoparticles in grey (for additional images see Supporting Information Figure SI-16). Cryo-TEM contrast being dependant of the electron density, the presence of a high electron density material, such as silver metal, strongly decreases the contrast between the two organic semiconductors. As a consequence, the Janus morphology appears harder to identify with the presence of silver. However, when the contrast is high enough, the images shows that silver mainly covered the PCBM domains, consistent with the energetic mechanism driving the photodeposition process. The presence of the silver metal was formally identified by Auger analysis (Figure 4c). Two distinct areas, 1 and 2, were targeted for the Auger analysis on the sample, area 1 being silver free and area 2 deposited silver organic semiconductor

nanoparticles. Several Auger elements were detected in the two spectra including sulphur (LVV transition at 130-160 eV), carbon (KLL transition at 180-290 eV) and oxygen (KLL transition at 455-530 eV), as expected for P3HT, $PC_{61}BM$ and F127 surfactant. However, only the area 2 revealed the presence of silver signal (MNN transition at 310-370 eV) attesting of the chemical detection of silver domains.[40–42]

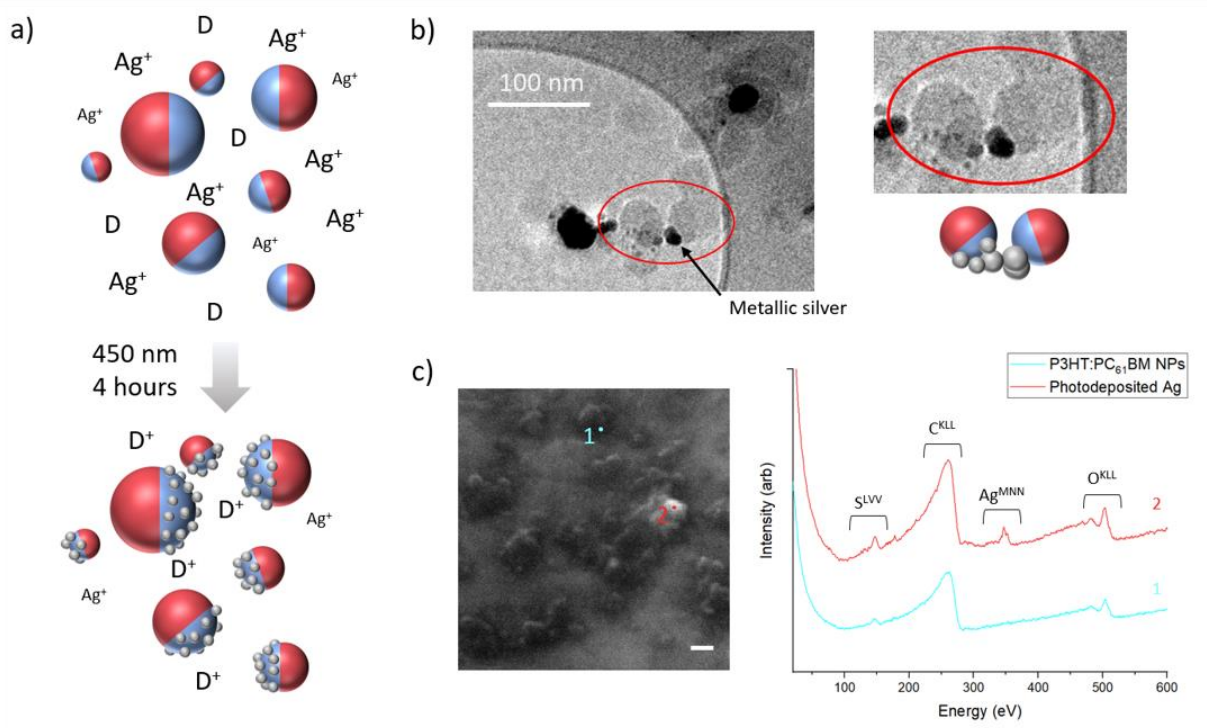

Figure 4. Schematic representation of silver photodeposition process from $AgNO_{3\,(aq)}$, from P3HT:$PC_{61}BM$ Janus nanoparticles (F127, Table 1, Entry 4) with methanol as the sacrificial donor "D" (a). Cryo-TEM images of Janus nanoparticles after photodeposition (b). Auger spectra of dots 1 and 2 on SEM image (left) of P3HT:$PC_{61}BM$ nanoparticles after silver photodeposition (c). Scale bars are 100 nm.

4. Conclusion

In summary, we report, for the first time, the preparation of Janus nanoparticles from organic semiconducting materials P3HT:$PC_{61}BM$ by a simple and one-step process, nanoprecipitation. The conjugated materials were dissolved in THF and then precipitated in water containing a surfactant such as SDS or Pluronic F127, or without any surfactant. High resolution cryo-TEM allowed to identify this morphology which was further confirmed by STXM. This morphology is driven by a low difference between surface tensions ratios ($\gamma_{PCBM/Liq}/\gamma_{P3HT/PCBM}$ and $\gamma_{P3HT/Liq}/\gamma_{P3HT/PCBM)}$ and in accordance with modelling reports. The nanoparticles absorb light from 200 to 650 nm and the $PC_{61}BM$ face effectively quenches the P3HT photoluminescence. Two sets of preliminary experiments were performed to reveal the potential use of these nanoparticles for photovoltaics or photocatalytic reactions. Firstly, OFETs were fabricated with P3HT:$PC_{61}BM$ Janus NP water-based dispersion and the mobilities measured were found to be close to that of P3HT:$PC_{61}BM$ OFET devices fabricated from traditional bulk heterojunction organic solutions, indicating efficient transport between the P3HT domains. These particles could be of high interest in PV as they present high exciton dissociation yield together with large charge percolation pathways provided by the Janus morphology. Secondly, we demonstrated that the irradiation of nanoparticles in the presence of a silver salt ($AgNO_{3(aq)}$), could lead to the photodeposition of silver metal nanoparticles. We believe that such Janus morphology, with the two materials acting as the cathode and the anode, and in which H^+ or CO_2 reduction can occur at one side of the nanoparticle and oxidation can take place at the other side, is a promising new candidate for photocatalysis.

Data availability statement

The data sets generated and/or analysed during the present study are available from the corresponding author upon reasonable request.

Acknowledgements

The authors thank E2S UPPA for funding the research. The PolLux end station at the Swiss Light Source synchrotron was financed by the German Minister für Bildung und Forschung (BMBF) through contracts 05K16WED and 05K19WE2. The authors acknowledge the support provided by the ANR through the WATER-PV project N°ANR-20-CE05-0002-01. The authors acknowledge the technical and scientific assistance of Sydney Microscopy & Microanalysis, the University of Sydney node of Microscopy Australia. We further thank the support of the University of Sydney Core Research Facilities. The University of Newcastle Electron Microscopy and X-ray (EMX) Unit is acknowledged for providing access to electron microscopes and associated expertise. The authors gratefully acknowledge Christophe Chassenieux from the Institute of Molecules and Macromolecules of Le Mans (IMMM, UMR 6283) for the fuitful discussions and financial support of a part of the Cryo-TEM measurements. The work at University of Tokyo has been supported by KAKENHI from JSPS (JP20H05660)

References

[1] K.A. Mazzio, C.K. Luscombe, The future of organic photovoltaics, Chem. Soc. Rev. 44 (2015) 78–90. https://doi.org/10.1039/C4CS00227J.

[2] O. Almora, D. Baran, G.C. Bazan, C. Berger, C.I. Cabrera, K.R. Catchpole, S. Erten-Ela, F. Guo, J. Hauch, A.W.Y. Ho-Baillie, T.J. Jacobsson, R.A.J. Janssen, T. Kirchartz, N. Kopidakis, Y. Li, M.A. Loi, R.R. Lunt, X. Mathew, M.D. McGehee, J. Min, D.B. Mitzi, M.K. Nazeeruddin, J. Nelson, A.F. Nogueira, U.W. Paetzold, N. Park, B.P. Rand, U. Rau, H.J. Snaith, E. Unger, L. Vaillant-Roca, H. Yip, C.J. Brabec, Device Performance of Emerging Photovoltaic Materials (Version 2), Advanced Energy Materials. 11 (2021) 2102526. https://doi.org/10.1002/aenm.202102526.

[3] N. Fajrina, M. Tahir, A critical review in strategies to improve photocatalytic water splitting towards hydrogen production, International Journal of Hydrogen Energy. 44 (2019) 540–577. https://doi.org/10.1016/j.ijhydene.2018.10.200.

[4] M.R. Singh, A.T. Bell, Design of an artificial photosynthetic system for production of alcohols in high concentration from CO_2, Energy Environ. Sci. 9 (2016) 193–199. https://doi.org/10.1039/C5EE02783G.

[5] N. Cox, D.A. Pantazis, F. Neese, W. Lubitz, Artificial photosynthesis: understanding water splitting in nature, Interface Focus. 5 (2015) 20150009. https://doi.org/10.1098/rsfs.2015.0009.

[6] N.P. Holmes, S. Chambon, A. Holmes, X. Xu, K. Hirakawa, E. Deniau, C. Lartigau-Dagron, A. Bousquet, Organic semiconductor colloids: From the knowledge acquired in

photovoltaics to the generation of solar hydrogen fuel, Current Opinion in Colloid & Interface Science. 56 (2021) 101511. https://doi.org/10.1016/j.cocis.2021.101511.
[7] J. Kosco, M. Bidwell, H. Cha, T. Martin, C.T. Howells, M. Sachs, D.H. Anjum, S. Gonzalez Lopez, L. Zou, A. Wadsworth, W. Zhang, L. Zhang, J. Tellam, R. Sougrat, F. Laquai, D.M. DeLongchamp, J.R. Durrant, I. McCulloch, Enhanced Photocatalytic Hydrogen Evolution from Organic Semiconductor Heterojunction Nanoparticles, Nature Materials. 19 (2020) 559–565. https://doi.org/10.1038/s41563-019-0591-1.
[8] J. Kosco, S. Gonzalez-Carrero, C.T. Howells, T. Fei, Y. Dong, R. Sougrat, G.T. Harrison, Y. Firdaus, R. Sheelamanthula, B. Purushothaman, F. Moruzzi, W. Xu, L. Zhao, A. Basu, S. De Wolf, T.D. Anthopoulos, J.R. Durrant, I. McCulloch, Generation of long-lived charges in organic semiconductor heterojunction nanoparticles for efficient photocatalytic hydrogen evolution, Nat Energy. 7 (2022) 340–351. https://doi.org/10.1038/s41560-022-00990-2.
[9] A. Holmes, E. Deniau, C. Lartigau-Dagron, A. Bousquet, S. Chambon, N.P. Holmes, Review of Waterborne Organic Semiconductor Colloids for Photovoltaics, ACS Nano. (2021) acsnano.0c10161. https://doi.org/10.1021/acsnano.0c10161.
[10] B.A. Pinaud, J.D. Benck, L.C. Seitz, A.J. Forman, Z. Chen, T.G. Deutsch, B.D. James, K.N. Baum, G.N. Baum, S. Ardo, H. Wang, E. Miller, T.F. Jaramillo, Technical and economic feasibility of centralized facilities for solar hydrogen production via photocatalysis and photoelectrochemistry, Energy Environ. Sci. 6 (2013) 1983. https://doi.org/10.1039/c3ee40831k.
[11] L. Dou, J. You, Z. Hong, Z. Xu, G. Li, R.A. Street, Y. Yang, 25th Anniversary Article: A Decade of Organic/Polymeric Photovoltaic Research, Adv. Mater. 25 (2013) 6642–6671. https://doi.org/10.1002/adma.201302563.
[12] G.J. Hedley, A.J. Ward, A. Alekseev, C.T. Howells, E.R. Martins, L.A. Serrano, G. Cooke, A. Ruseckas, I.D.W. Samuel, Determining the optimum morphology in high-performance polymer-fullerene organic photovoltaic cells, Nat Commun. 4 (2013) 2867. https://doi.org/10.1038/ncomms3867.
[13] S. Yoon, E.-Y. Shin, N.-K. Cho, S. Park, H.Y. Woo, H.J. Son, Progress in morphology control from fullerene to nonfullerene acceptors for scalable high-performance organic photovoltaics, J. Mater. Chem. A. 9 (2021) 24729–24758. https://doi.org/10.1039/D1TA06861J.
[14] N.P. Holmes, M. Marks, P. Kumar, R. Kroon, M.G. Barr, N. Nicolaidis, K. Feron, A. Pivrikas, A. Fahy, A. Diaz De Zerio Mendaza, A.L.D. Kilcoyne, C. Müller, X. Zhou, M.R. Andersson, P.C. Dastoor, W.J. Belcher, Nano-pathways: Bridging the Divide Between Water-processable Nanoparticulate and Bulk Heterojunction Organic Photovoltaics, Nano Energy. 19 (2016) 495–510. https://doi.org/10.1016/j.nanoen.2015.11.021.
[15] N.P. Holmes, N. Nicolaidis, K. Feron, M. Barr, K.B. Burke, M. Al-Mudhaffer, P. Sista, A.L.D. Kilcoyne, M.C. Stefan, X. Zhou, P.C. Dastoor, W.J. Belcher, Probing the origin of photocurrent in nanoparticulate organic photovoltaics, Solar Energy Materials and Solar Cells. 140 (2015) 412–421. https://doi.org/10.1016/j.solmat.2015.04.044.
[16] M.G. Barr, S. Chambon, A. Fahy, T.W. Jones, M.A. Marcus, A.L.D. Kilcoyne, P.C. Dastoor, M.J. Griffith, N.P. Holmes, Nanomorphology of eco-friendly colloidal inks, relating non-fullerene acceptor surface energy to structure formation, Mater. Chem. Front. 5 (2021) 2218–2233. https://doi.org/10.1039/D0QM00980F.
[17] S. Ulum, N. Holmes, M. Barr, A.L.D. Kilcoyne, B. Bin Gong, X. Zhou, W. Belcher, P. Dastoor, The role of miscibility in polymer:fullerene nanoparticulate organic photovoltaic devices, Nano Energy. 2 (2013) 897–905. https://doi.org/10.1016/j.nanoen.2013.03.009.
[18] T.S. Gehan, M. Bag, L.A. Renna, X. Shen, D.D. Algaier, P.M. Lahti, T.P. Russell, D. Venkataraman, Multiscale active layer morphologies for organic photovoltaics through

self-assembly of nanospheres, Nano Letters. 14 (2014) 5238–5243. https://doi.org/10.1021/nl502209s.
[19] D. Darwis, N. Holmes, D. Elkington, A.L. David Kilcoyne, G. Bryant, X. Zhou, P. Dastoor, W. Belcher, Surfactant-free nanoparticulate organic photovoltaics, Solar Energy Materials and Solar Cells. 121 (2014) 99–107. https://doi.org/10.1016/j.solmat.2013.10.010.
[20] C. Xie, X. Tang, M. Berlinghof, S. Langner, S. Chen, A. Späth, N. Li, R.H. Fink, T. Unruh, C.J. Brabec, Robot-based high-throughput engineering of alcoholic polymer: Fullerene nanoparticle inks for an eco-friendly processing of organic solar cells, ACS Applied Materials and Interfaces. 10 (2018) 23225–23234. https://doi.org/10.1021/acsami.8b03621.
[21] G. Prunet, L. Parrenin, E. Pavlopoulou, G. Pecastaings, C. Brochon, G. Hadziioannou, E. Cloutet, Aqueous PCDTBT:PC $_{71}$ BM Photovoltaic Inks Made by Nanoprecipitation, Macromol. Rapid Commun. 39 (2018) 1700504. https://doi.org/10.1002/marc.201700504.
[22] C.J. Martínez Rivas, M. Tarhini, W. Badri, K. Miladi, H. Greige-Gerges, Q.A. Nazari, S.A. Galindo Rodríguez, R.Á. Román, H. Fessi, A. Elaissari, Nanoprecipitation process: From encapsulation to drug delivery, International Journal of Pharmaceutics. 532 (2017) 66–81. https://doi.org/10.1016/j.ijpharm.2017.08.064.
[23] C. Xie, T. Heumüller, W. Gruber, X. Tang, A. Classen, I. Schuldes, M. Bidwell, A. Späth, R.H. Fink, T. Unruh, I. McCulloch, N. Li, C.J. Brabec, Overcoming efficiency and stability limits in water-processing nanoparticular organic photovoltaics by minimizing microstructure defects, Nat Commun. 9 (2018) 5335. https://doi.org/10.1038/s41467-018-07807-5.
[24] Y. Sun, Y. Han, J. Liu, Controlling PCBM aggregation in P3HT/PCBM film by a selective solvent vapor annealing, Chin. Sci. Bull. 58 (2013) 2767–2774. https://doi.org/10.1007/s11434-013-5944-6.
[25] V. Chaudhary, R.K. Pandey, R. Prakash, N. Kumar, A.K. Singh, Highly aligned and crystalline poly(3-hexylthiophene) thin films by off-center spin coating for high performance organic field-effect transistors, Synthetic Metals. 258 (2019) 116221. https://doi.org/10.1016/j.synthmet.2019.116221.
[26] X. Yan, J. Bernard, F. Ganachaud, Nanoprecipitation as a simple and straightforward process to create complex polymeric colloidal morphologies, Advances in Colloid and Interface Science. 294 (2021) 102474. https://doi.org/10.1016/j.cis.2021.102474.
[27] C. Sosa, R. Liu, C. Tang, F. Qu, S. Niu, M.Z. Bazant, R.K. Prud'homme, R.D. Priestley, Soft Multifaced and Patchy Colloids by Constrained Volume Self-Assembly, Macromolecules. 49 (2016) 3580–3585. https://doi.org/10.1021/acs.macromol.6b00708.
[28] T. Higuchi, A. Tajima, H. Yabu, M. Shimomura, Spontaneous formation of polymer nanoparticles with inner micro-phase separation structures, Soft Matter. 4 (2008) 1302. https://doi.org/10.1039/b800904j.
[29] N. Li, A.Z. Panagiotopoulos, A. Nikoubashman, Structured Nanoparticles from the Self-Assembly of Polymer Blends through Rapid Solvent Exchange, Langmuir. 33 (2017) 6021–6028. https://doi.org/10.1021/acs.langmuir.7b00291.
[30] J. Aubry, F. Ganachaud, J.-P. Cohen Addad, B. Cabane, Nanoprecipitation of Polymethylmethacrylate by Solvent Shifting:1. Boundaries, Langmuir. 25 (2009) 1970–1979. https://doi.org/10.1021/la803000e.
[31] E. Lepeltier, C. Bourgaux, P. Couvreur, Nanoprecipitation and the "Ouzo effect": Application to drug delivery devices, Advanced Drug Delivery Reviews. 71 (2014) 86–97. https://doi.org/10.1016/j.addr.2013.12.009.

[32] I.J. Joye, D.J. McClements, Production of nanoparticles by anti-solvent precipitation for use in food systems, Trends in Food Science & Technology. 34 (2013) 109–123. https://doi.org/10.1016/j.tifs.2013.10.002.
[33] J. Shen, J. Wu, M. Wang, P. Dong, J. Xu, X. Li, X. Zhang, J. Yuan, X. Wang, M. Ye, R. Vajtai, J. Lou, P.M. Ajayan, Surface Tension Components Based Selection of Cosolvents for Efficient Liquid Phase Exfoliation of 2D Materials, Small. 12 (2016) 2741–2749. https://doi.org/10.1002/smll.201503834.
[34] J. Raabe, G. Tzvetkov, U. Flechsig, M. Böge, A. Jaggi, B. Sarafimov, M.G.C. Vernooij, T. Huthwelker, H. Ade, D. Kilcoyne, T. Tyliszczak, R.H. Fink, C. Quitmann, PolLux: A new facility for soft x-ray spectromicroscopy at the Swiss Light Source, Review of Scientific Instruments. 79 (2008) 113704. https://doi.org/10.1063/1.3021472.
[35] K.N. Schwarz, S.B. Farley, T.A. Smith, K.P. Ghiggino, Charge generation and morphology in P3HT : PCBM nanoparticles prepared by mini-emulsion and reprecipitation methods, Nanoscale. 7 (2015) 19899–19904. https://doi.org/10.1039/C5NR06244F.
[36] G. Horowitz, Organic Field-Effect Transistors, Adv. Mater. 10 (1998) 365–377. https://doi.org/10.1002/(SICI)1521-4095(199803)10:5<365::AID-ADMA365>3.0.CO;2-U.
[37] M. Morana, P. Koers, C. Waldauf, M. Koppe, D. Muehlbacher, P. Denk, M. Scharber, D. Waller, C. Brabec, Organic Field-Effect Devices as Tool to Characterize the Bipolar Transport in Polymer-Fullerene Blends: The Case of P3HT-PCBM, Adv. Funct. Mater. 17 (2007) 3274–3283. https://doi.org/10.1002/adfm.200700124.
[38] R. Szymanski, R. Henry, S. Stuard, U. Vongsaysy, S. Courtel, L. Vellutini, M. Bertrand, H. Ade, S. Chambon, G. Wantz, Balanced Charge Transport Optimizes Industry-Relevant Ternary Polymer Solar Cells, Sol. RRL. 4 (2020) 2000538. https://doi.org/10.1002/solr.202000538.
[39] C. Pacholski, A. Kornowski, H. Weller, Site-Specific Photodeposition of Silver on ZnO Nanorods, Angew. Chem. Int. Ed. 43 (2004) 4774–4777. https://doi.org/10.1002/anie.200453880.
[40] S. Bera, P. Gangopadhyay, K.G.M. Nair, B.K. Panigrahi, S.V. Narasimhan, Electron spectroscopic analysis of silver nanoparticles in a soda-glass matrix, Journal of Electron Spectroscopy and Related Phenomena. 152 (2006) 91–95. https://doi.org/10.1016/j.elspec.2006.03.008.
[41] R. Ambroziak, M. Hołdyński, T. Płociński, M. Pisarek, A. Kudelski, Cubic Silver Nanoparticles Fixed on TiO2 Nanotubes as Simple and Efficient Substrates for Surface Enhanced Raman Scattering, Materials. 12 (2019) 3373. https://doi.org/10.3390/ma12203373.
[42] J.B. Ledeuil, A. Uhart, S. Soulé, J. Allouche, J.C. Dupin, H. Martinez, New insights into micro/nanoscale combined probes (nanoAuger, μXPS) to characterize Ag/Au@SiO_2 core–shell assemblies, Nanoscale. 6 (2014) 11130–11140. https://doi.org/10.1039/C4NR03211J.